

Highly Reliable BaTiO₃-Polyphenylene Oxide Nanocomposite Dielectrics via Cold Sintering

Takao Sada, Kosuke Tsuji, Arnaud Ndayishimiye, Zhongming Fan, Yoshihiro Fujioka, and Clive A. Randall*

In the design of the ceramic capacitor, high capacitance, temperature stability, and high operating voltage must be balanced against the failure mechanisms of degradation. Cold sintering is used to develop dense BaTiO₃ – poly (p-phenylene oxide) (PPO) nanocomposites with PPO throughout the grain boundary microstructure. To obtain the desired PPO distribution, a process is introduced that distributes the polymers on the BaTiO₃ powders prior to the cold sintering process. With the cold sintering enabled by a Ba(OH)₂·8H₂O transient phase, theoretical densities ≈95% could be obtained at a sintering temperature ≈225 °C with up to 15 vol% PPO content. The rationale is to influence the local electric field distribution within the dielectric, to maximize resistivity (10¹³–10¹⁴ Ω cm) and degradation resistance, minimize temperature dependence of permittivity, and minimize the field dependent permittivity. All these properties are investigated as a function of the volume fraction of PPO. The magnitude of the permittivity follows a logarithmic mixing law: 1460 to 680 for the nanocomposite with 5 to 15 vol% PPO content, respectively, at room temperature. The BaTiO₃-PPO composite dielectrics are contrasted under accelerated lifetime testing conditions, noting superior resistance toward degradation kinetics, indicating an important breakthrough opportunity towards the development of high reliability dielectrics.

has been great insight gained into the mechanism, doping, and possible composite designs in ceramics, polymers, and polymer-ceramic composites, all driving instantaneous breakdown strength and electrostatic energy densities.^[4–6] It is important in designing such dielectrics to understand the dielectric properties, the dielectric strength, the resistivity, and the degradation mechanisms. In many materials, these degradation and breakdown processes limit the material adoption by industry. Capacitor devices are the weakest electrical component in a system, and the failure of such a device can be catastrophic to a system. Therefore, these types of capacitors require a derating to ensure that their operational lifetimes do not limit the lifetimes of the whole electric subsystem.

Many researchers concern themselves with the temperature dependence of a dielectric material, and energy density limits for short periods of time, but for these dielectrics to be useful in ceramic-based capacitors, they must operate reliably under high electric fields and

temperatures. Under these conditions, the electromigration of ionic species (mostly oxygen vacancies) can control the degradation and the mean time to failure. The methods to limit this process are through dopants, microstructural control, and grain boundary barriers. Details of this process can be found in a series of important publications from Waser et al., and others.^[7–9] A few major challenges occur with the technological trends with BaTiO₃-based multilayer capacitors; these include the mean time to failure under high bias and temperature with thinner dielectric layers. Despite these challenges, both in terms of reliability and cost constraints, there has been a Moore's law progress in volumetric capacitive efficiency over the last two decades.^[10] This was accomplished with many advances in understanding the compositional design, defect chemistry, defect dynamics, the electrode and dielectric powder development, the forming process technology, and the fast-firing process.^[11–15]

To disrupt such a robust and excellent technology associated with BaTiO₃-based multilayer capacitors, we either need to discover a new high dielectric permittivity material that can provide the high performance and reliability, or

1. Introduction

There is an urgent need to develop higher performance electronic capacitive devices that will enable high voltage and high temperature operations, while maintaining the dielectric properties against aging phenomena, such as degradation of insulative resistance and dielectric breakdown.^[1–3] There

T. Sada, Y. Fujioka
Monozukuri R&D Laboratory
KYOCERA Corporation
Kirishima, Kagoshima 899-4312, Japan

T. Sada, K. Tsuji, A. Ndayishimiye, Z. Fan, C. A. Randall
Materials Research Institute and Department of Materials Science & Engineering
The Pennsylvania State University
University Park, PA 16802, USA
E-mail: car4@psu.edu

 The ORCID identification number(s) for the author(s) of this article can be found under <https://doi.org/10.1002/admi.202100963>.

DOI: 10.1002/admi.202100963

we need to consider new types of composite design and/or a new processing approach that enables all the above. The strategies around the world have been the search for new materials, either new dielectric compositions or nanocomposites, but these have been limited to drop-in technologies around traditional processes.^[16,17] Recently, we have introduced a new sintering process that is enabling the densification of ceramics and ceramic-polymer composites across a large family of material types that can impact many fields of research.^[18] This process has been termed cold sintering; it involves the use of a transient chemical phase in which, with the assistance of an applied pressure and low temperatures <300 °C, the materials can undergo densification. Apart from the industrial advantages, such as lower costs thanks to the use of base metals as electrodes,^[19] and reduced energy consumption,^[20–22] the unprecedented low-temperature process allows us to develop the new type of ceramic-based composites utilizing advantages of the composed materials.^[23,24] If what we will demonstrate below is embraced by the community, there are many opportunities to combine the new dielectrics, both polymers and ceramics, and process them to control the local electric fields and limit the semiconducting and degradation processes that limit the new materials into industry, replacing the all-important BaTiO₃ based dielectric materials. Having said that, we have chosen to demonstrate these new opportunities with the BaTiO₃ dielectric as a starting point.

Current progress in the cold sintering has also enabled the co-sintering of dense BaTiO₃ dielectrics with polymer, where polytetrafluorethylene (PTFE) was used for the first demonstration, using alkaline flux as a transient chemical phase.^[25,26] Typically, conventional polymer-based composites with high permittivity ceramic fillers had relatively low permittivity (less than 100) in the effective volume fraction range (mostly < 60 vol%) of ceramics because the pores and voids are incorporated in the range over 60 vol%.^[27–29] To overcome the low permittivity, artificial nanostructures, such as parallel connectivity (vertical aligned fillers), have been proposed, but it is not favorable for the reliability, since it easily forms the weakest path for a breakdown.^[30] With the cold sintering, BaTiO₃-PTFE composite exhibits the high density (≈95%), the high permittivity (≈1000), the diffuseness of the phase transition, the high resistivity, and the linear ac field dependence of the ferroelectric well beyond the coercive field of BaTiO₃.^[26] However, despite these attractive properties, cold sintered BaTiO₃-PTFE composite is still far from the practical applications for the capacitor materials because of the inhomogeneous distribution of the polymer that results in the low reliability. The incompatibility between polymers and ceramics leads to poor dispersion degree of polymers in the matrix. Since the breakdown happens at the weakest point,^[31,32] homogeneous distribution of polymers is a primary requirement to achieve highly reliable materials. Typically, for the conventional polymer-BaTiO₃ composites, there have been several researches on the interface design to improve the compatibility between them.^[33] For example, surface modification of BaTiO₃ with silane coupling agents^[34,35] or surfactants with various ligands, such as phosphonic acids,^[36,37] carboxylic acids,^[38,39] and hydroxyls,^[40,41] could provide better compatibility between

two phases and achieve improved properties of the composites. However, since the oxide surfaces should be reactive during the cold sintering, surface modification can be detrimental to the densification.^[42] The other useful approach is physical adsorption of polymer with bare ceramics without modifiers.^[43–45] A strong interaction of hydroxylated BaTiO₃ with poly(vinylidene fluoride) (PVDF) through hydrogen bonding is one of the most accepted approaches for the polymer-BaTiO₃ nanocomposites.^[43,44] However, it is noted that for the cold sintered BaTiO₃-based nanocomposite, the alkaline stability of polymers is also required, since the polymers are subjected to harsh chemical (molten flux) as well as high-pressure and temperature environments. PVDF is reported to decompose under high pH environment (PVDF was also decomposed under alkali-based CSP, data not shown).^[46] Thus, approaches to design and control of the interface for alkaline-based cold sintering of ceramic-polymer composites are highly desirable. Here, we report on the dense cold sintered BaTiO₃-polymer nanocomposite without compromising high permittivity and reliability through better compatibility and spatial distribution of the polymer phase. This is considered with an alternative process, and polymer chemistry, namely poly (p-phenylene oxide) (PPO).

2. Results and Discussion

2.1. Processing

Experimental procedures for CSP of BaTiO₃-PPO composites using Ba(OH)₂·8H₂O flux and chemical structure of PPO are shown in **Figure 1**. The adsorption of polymers on oxide surfaces can either be physical or chemical.^[47] The adsorbate molecule/adsorbent surface system is more stable for chemical adsorption, as covalent bonding does occur, and less stable for physical adsorption, as it involves weaker forces such as van der Waals interactions. Given the densification by cold sintering,^[48] the stiff and stable chemical adsorption can affect the interface-coupled dissolution-precipitation (Figure 1) kinetics, leading to lower relative densities. Indeed, the use of surfactants with chemical bonding sites impacts the kinetics of cold sintering reaction and decreases the permittivity of cold sintered BaTiO₃ (BT) dramatically.^[42] Therefore, we assume that the physical adsorption of polymer chains with multiple-point interactions is a better approach to design interfaces of cold sintered composites, without significantly affecting the efficiency of densification (Figure 1). To obtain physical adsorption, BT powders were first washed with acetic acid to deplete the surface of Ba²⁺ ions^[49] and provide surface hydroxyls.^[50,51] It is noted that hydroxylation by acid provides a surface with Brønsted acidic OH, whereas Brønsted-basic OH is formed by H₂O₂ treatment.^[50] There is no significant change in microstructures and size of the nanoparticles after acidic treatment, as shown in Figure S1a,b in the Supporting Information. On the other hand, the high magnification image of the acid-treated BaTiO₃ (AcBT) surface with transmission electron microscopy (TEM) reveals that the Ba²⁺ ions are incongruently extracted from the surface and leave behind an amorphous layer that is self-limited in a passivation process,

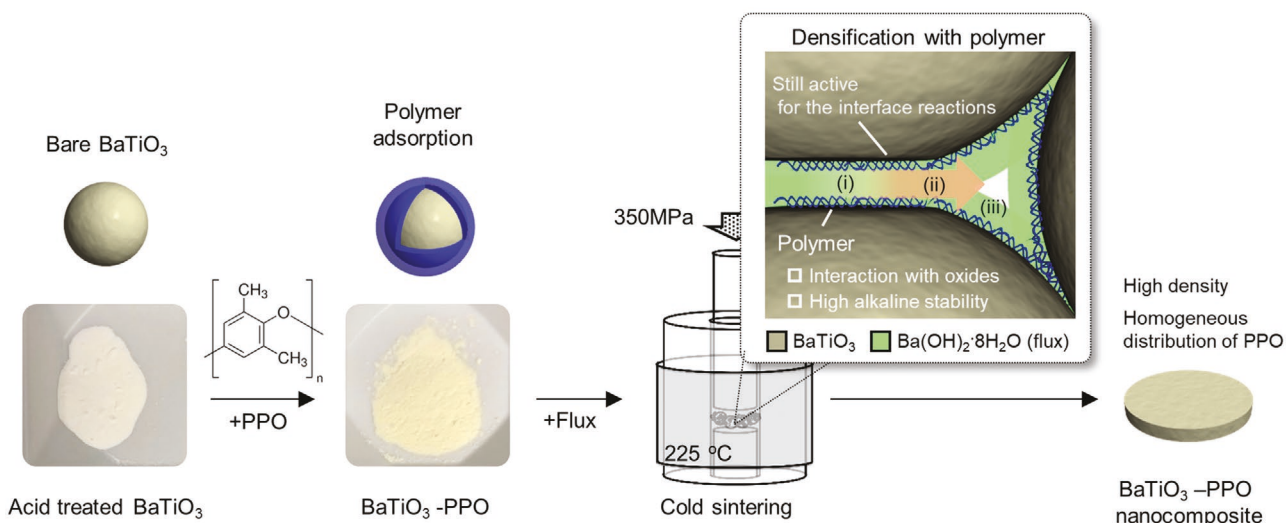


Figure 1. Scheme for fabrication of BT-PPO nanocomposites using cold sintering. PPO can adsorb on the surface of acid-treated BT through hydrogen bonding. The pressure-enhanced interface reactions i) dissolution, ii) diffusion, and iii) precipitation of dissolved ions in the inset image drives the densification even with adsorbed polymers at low temperature. Polymers have an appropriate interaction with oxides, which aids their homogenous distribution in the matrix without hindering chemical reactions at the interface.

thereby with appropriate control of the surfaces (**Figure 2a**). The thickness of the amorphous layer is approximately 5 nm, which is consistent with observations by Völtzke et al.^[49] This, in conventional synthesis, is avoided, as it perturbs the surface

crystallinity and stoichiometry, and these effects are typically harmful in controlling the microstructure of conventional sintered BaTiO₃. The use of a Ba(OH)₂·8H₂O transient phase not only drives the sintering process and allows for the low

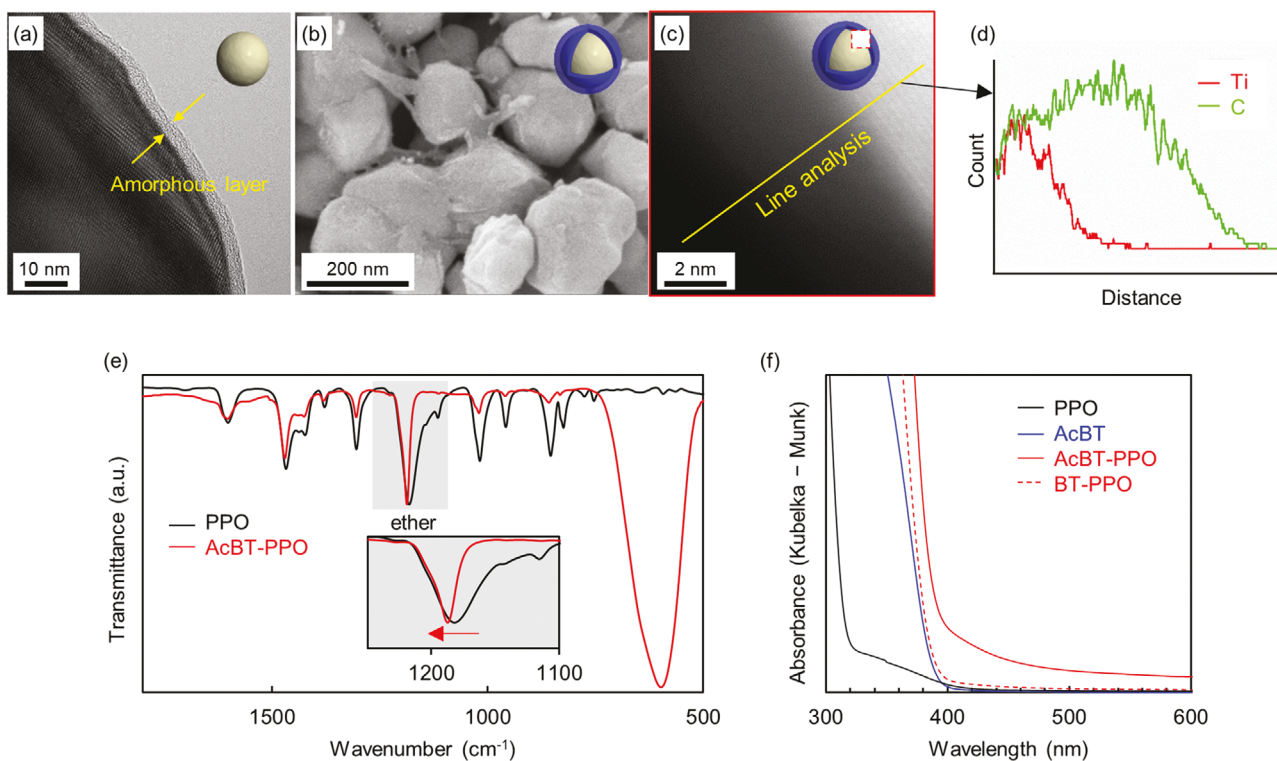


Figure 2. a) TEM micrograph of the acid-treated BT powders (AcBT) showing an amorphous surface ≈ 5 nm thick after the acid treatment. b) SEM image of AcBT after mixing with PPO and c) TEM image of the powders with PPO coatings on the particle surfaces. d) Further confirmation of the polymer at the surface is seen with the relative energy dispersive x-ray profiles in contrasting the inorganic Ti and C signals from the PPO coating. e) FTIR-ATR spectra of PPO and AcBT after mixing with PPO. f) UV-Vis absorption data plotted with the Kubelka-Munk function versus wavelength for PPO, AcBT, AcBT – PPO, and BT – PPO.

temperature densification, but it also compensates for the stoichiometry of the final materials.^[52]

The polymer (PPO) is mixed with AcBT in toluene. The choice of solvent is very crucial for the dispersion of the polymer in the matrix. Toluene is a good solvent for PPO and can dissolve the long-chains of the polymer,^[53,54] which can aid the formation of multiple point interaction with the surface using simple solution process. Scanning electron microscopy (SEM) image of AcBT-PPO powders indicates that polymers do not fully coat BT surfaces (Figure 2b), but are homogeneously distributed throughout the powder (Figure S1c, Supporting Information). High resolution transmission electron microscopy (TEM) analysis and corresponding energy dispersive spectroscopy (EDS) line profile also confirm the PPO adsorption on BT surfaces (Figure 2c,d). The Ti-rich surfaces on BT particles with surface hydroxyls could provide Brønsted acid sites,^[50] and the ether oxygen in the PPO is expected to act as a Lewis base, and thereby can interact with the interface through hydrogen bonding.^[55] This interaction is supported with both the FTIR spectra and the ultraviolet visible absorption spectroscopy, Figure 2e,f. There is a shift in the vibrational mode associated with the ether group (C-O-C linkage) consistent with interaction with oxides, permitting an adsorption of the polymer chain with the BT surface (Figure 2e).^[56] Furthermore, the UV-vis adsorption in the visible region appears for AcBT-PPO powders,

as shown in Figure 2f (pictures before and after mixing are shown in Figure 1), and this might be due to a charge transfer between PPO and AcBT. Since no absorption in the visible region was observed for BT-PPO, these results also indicates the effective adsorption of PPO on the AcBT. As a result, all the above data points to this simple solution mixing process providing a coating of PPO on the BT powders, with the goal of optimizing the overall distribution of the PPO prior to the sintering, as shown in Figure 2.

2.2. Cold Sintering of BaTiO₃-PPO Nanocomposites

The final relative densities of AcBT-PPO are considered with different amounts of PPO. Figure 3a shows that high relative densities between 96% and 98% can be obtained. Here, the relative density globally and slightly increases with PPO content. For other types of thermoplastic polymers, such as PTFE, a decrease of the relative density with the amount of polymer is observed (Figure S2, Supporting Information). Since PTFE segregates and forms the aggregation easily, pores and voids could be incorporated, resulting in a lower relative density with the amount of polymer in the system.^[26,57,58] This suggests that PPO does not hinder the interface reaction and the following densification, regardless of the polymer amount. Given these

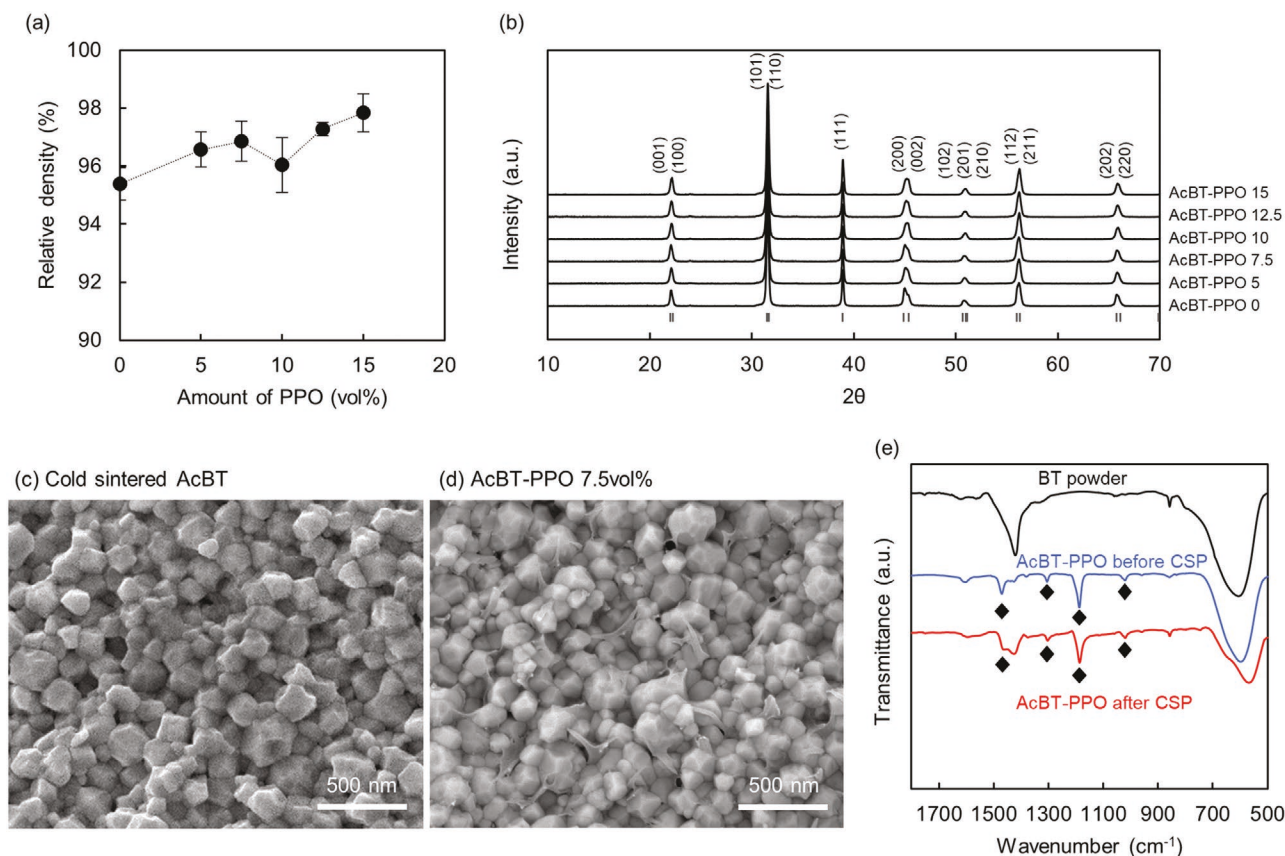


Figure 3. a) Relative density and b) XRD patterns of the cold sintered AcBT – PPO composites with 0, 5, 7.5, 10, 12.5, and 15 vol% PPO. Reference peak positions of BaTiO₃ are shown in black bars (PDF# 04-015-6089). SEM images of c) cold sintered AcBT, and d) AcBT-PPO nanocomposite with 7.5 vol% PPO. e) FTIR-ATR spectra of BaTiO₃ powders (black line), and the composites with 5 vol% PPO before (blue line) and after (red line) cold sintering.

differences between PTFE and PPO, one of the general criterion for selecting a specific polymer is not only to obtain high dense nanocomposites, but also to have a good dispersion characteristics of the polymer in ceramics along nearly all the grain boundaries. X-ray diffraction (XRD) patterns of cold sintered AcBT and AcBT-PPO composites only display diffraction peaks of a phase pure BT, without obvious impurities (Figure 3b). Figure 3c,d shows SEM images of cold sintered AcBT with 0 and 75 vol% PPO, both depicting dense microstructures with polygonal facets BT grains. In the presence of PPO, stretched polymers are also confirmed around the BT grain in the representative SEM image (Figure 3d). Similar dense microstructures with stretched polymers are also observed for all samples with different volume fractions of PPO (Figure S3a–f, Supporting Information). Grain sizes slightly decrease with the amount of PPO, but within a narrow range from 153 ± 47 and 169 ± 49 nm, as shown in Figure S4 in the Supporting Information. Low magnification SEM images in Figure S5 in the Supporting Information confirm that the polymers have a better homogeneous distribution in the AcBT – PPO nanocomposites, compared to the case of BT-PPO nanocomposites (without acid treatment), pointing to the importance of powder processing. This is probably due to the difference in the interaction between BT and PPO, as discussed above. To investigate the thermal and alkaline stability of PPO after CSP, initial BT powders with and without PPO, and the cold sintered AcBT-PPO composite, are studied by FTIR in Figure 3e. After mixing with PPO, characteristic bands of PPO appear at 1020, 1187, 1305, and 1470 cm^{-1} .^[56] These peaks are also observed after cold sintering, suggesting that the molecular integrity of the PPO can be retained during the CSP process. The PPO backbone is reported to possess strong alkaline stability in the field of alkaline fuel cell.^[59] Therefore, it is reasonable, but interesting to preserve the molecular structures under high temperature and high basicity levels. These results suggest that dense and phase pure BT with better compatibility and spatial distribution of the polymer phase are successfully fabricated using AcBT as starting powders.

2.3. Electrical Characterization of Cold Sintered BaTiO₃-PPO Composites

Figure 4a,b shows the temperature dependence of the dielectric permittivity and dielectric loss as a function of PPO amount in the densified composites. There is a systematic decrease in the room temperature permittivity as a function of the PPO volume fraction (Figure 4c). The variation was analyzed with the room temperature dielectric permittivity and found to follow the logarithmic law, which is the limiting case of the general mixing law^[23]

$$\bar{\epsilon}^n = \sum_{i=1} f_i \epsilon_i^n \quad (1)$$

where $\bar{\epsilon}$ is the average permittivity, f_i is the volume fraction of the i^{th} phase, ϵ_i is the relative permittivity of the i^{th} phase, and n is the exponent, $-1 \leq n \leq +1$. The exponent, n , is influenced by the spatial connectivity of each of the phases, as at the extremes: $n = +1$ is the parallel connectivity, $n = -1$ is the serial

connectivity, and $n = 0$ is an equal weighted mixture of parallel and serial connectivity (Figure 4c).^[23] The best fitting to the AcBT-PPO nanocomposite gives $n = 0$, the logarithmic mixing law, within this study, as shown in Figure 4c. This contrasts with the earlier work, where BT-PTFE matched to $n = -0.24$,^[26] and so here we have evidence that the spatial distribution of the PPO is more evenly distributed around each of the grains. The $n \approx 0$ limits with the 50% mixture of both serial and parallel connectivity, so this would be consistent with a uniform distribution of the polymers around each face of a grain. The logarithmic mixing law works well for average composite permittivities at all temperatures, including room temperature, and the T_{max} , and over the various volume fractions. The temperature dependences and the magnitudes of the permittivity are higher in the AcBT-PPO case, relative to the earlier BT-PTFE composites. We note that there is a decrease in the permittivity maxima, and an increase in diffuseness of the phase transition, but unlike the PTFE case the paraelectric-ferroelectric temperature did not shift with the increase in volume fraction of PPO (Figure S6, Supporting Information). These trends were also previously linked to ferroelectric size effects associated with precipitation of nano-BT particles and polarization gradients in the surfaces of the BT grains.^[26] Figure 4d shows changes in the loss tangent with time. There is a large increase in the loss tangent for cold sintered BT, whereas no significant change is observed for AcBT-PPO nanocomposites. Since hydroxide is used as a flux for cold sintering, residual Ba(OH)₂ at grain boundaries (G.B.) can be influenced by H₂O in the atmosphere, leading to such instability of the loss tangent. However, interestingly, we found that PPO at the grain boundary is also beneficial to the stability of the dielectric properties. In the BT-PTFE case, there is still a small variation with time. These results imply that the homogeneous distribution of hydrophobic polymer can prevent the reaction with H₂O, resulting in stable dielectric properties.

Figure 5a shows a schematic that represents the distribution of the microstructure with nanometer-scale polymer layers at the grain boundaries, and the voltage drop across the dielectric, and the gradients of voltage, that produce the localized electric field distribution enhancing at the polymer grain boundaries. The PPO in the grain boundaries perturbs the electric field strength distribution through the microstructure. The local electric field will be concentrated in the grain boundary relative to the grain, and this distribution can be considered from the continuity of the displacement field vector, D . This effect can be easily understood with the normal displacement field, D_{ni} in the i^{th} phase, and is continuous between both dielectric materials (BaTiO₃ grain and polymer at the grain boundary), $D_{ni} = \epsilon_g \epsilon_0 E_g = \epsilon_{gb} \epsilon_0 E_{gb}$. So, the local field in the BaTiO₃ ($\epsilon_g \approx 10^3$), E_g , is now reduced by $\approx 10^3$ times relative to the field in the polymer phase (grain boundary), E_{gb} , as a simple representation across a serially orientated grain and grain boundary relative to the applied electric field (Figure 5a). This, in turn, decreases the field in the BaTiO₃ grains and thereby limits the high field suppression of the permittivity, which reduces substantially the permittivity when field approaches and exceeds the coercive fields in ferroelectric materials, a phenomenon often referred to in ferroelectric capacitors as the voltage saturation effect. Figure 5b exhibits representative polarization-field (P-E) hysteresis loops with different applied fields for AcBT-PPO

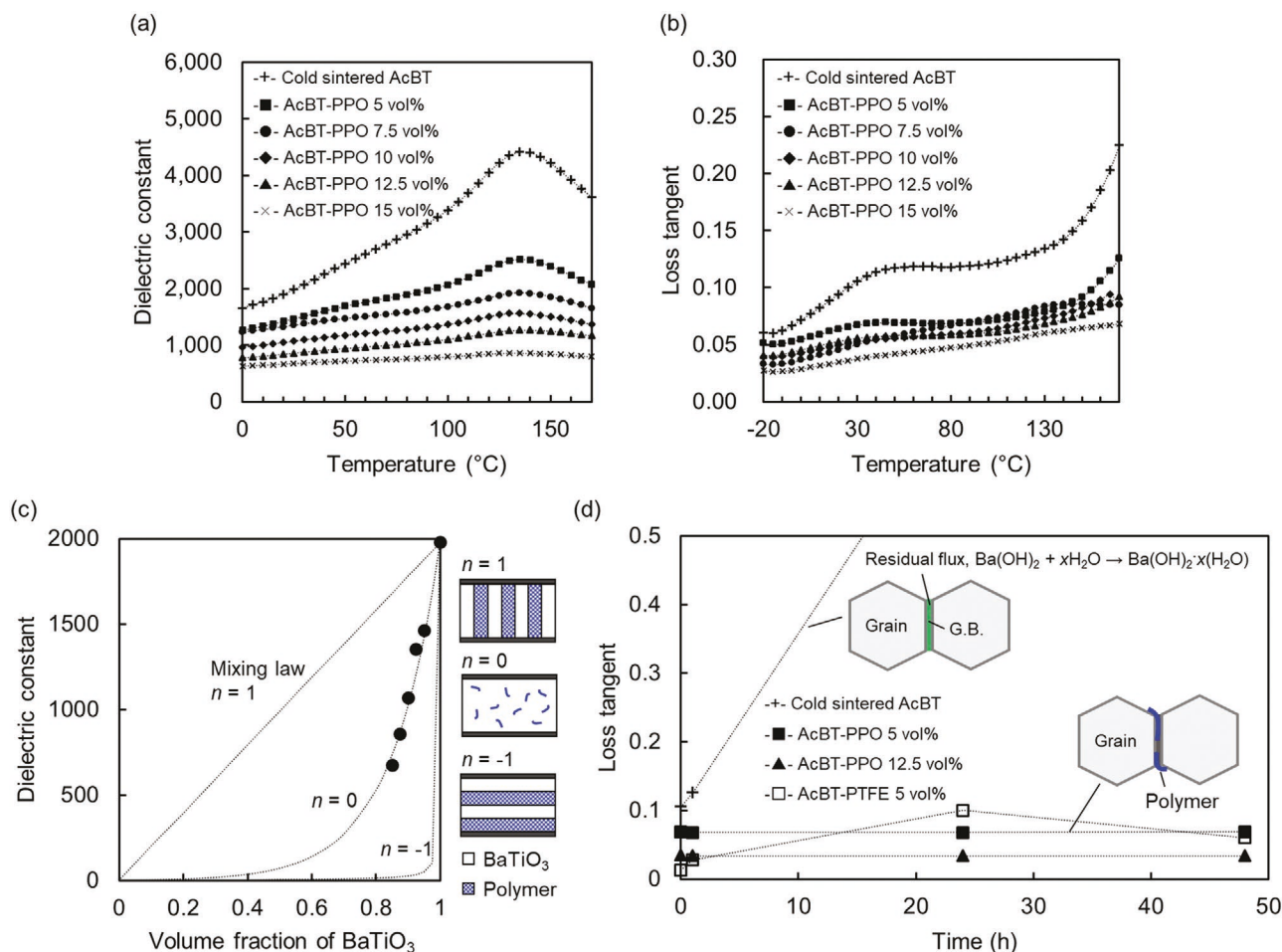


Figure 4. a) The relative permittivity, and b) loss tangent as a function of temperature between 0 and 170 °C, at 1 kHz, for the composites with 0, 5, 7.5, 10, 12.5 and 15 vol% PPO, and c) systematic variation of the room temperature relative permittivity, with the dotted line being the mixing law with $n = +1, 0, -1$. Schematic illustration of connectivity patterns at given n is shown on the right side. d) Changes in the loss tangent at 1 kHz for the composites with 0, 5, 12.5 vol% PPO and 5 vol% PTFE under ambient conditions.

nanocomposite, and this is used for the estimation of the field dependence of the permittivity. The voltage saturation effect is

greatly suppressed, as can be shown in Figure 5c, in dielectric nanocomposites with PPO volume fractions between 7.5, 10,

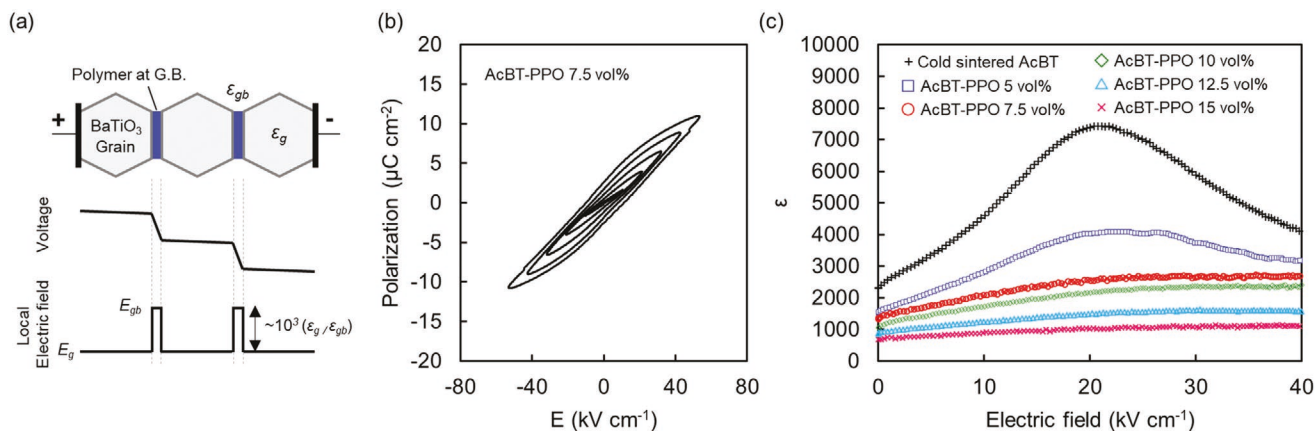


Figure 5. a) Schematic illustration of BaTiO₃ grains and polymer grain boundaries (G.B.). The corresponding voltage drop and electric field distribution across the microstructure are also shown. b) P-E hysteresis loop, at 100 Hz, for the composite with 7.5 vol% PPO. c) Field dependence of the permittivity for the composites with 0, 5, 7.5, 10, 12.5, and 15 vol% PPO.

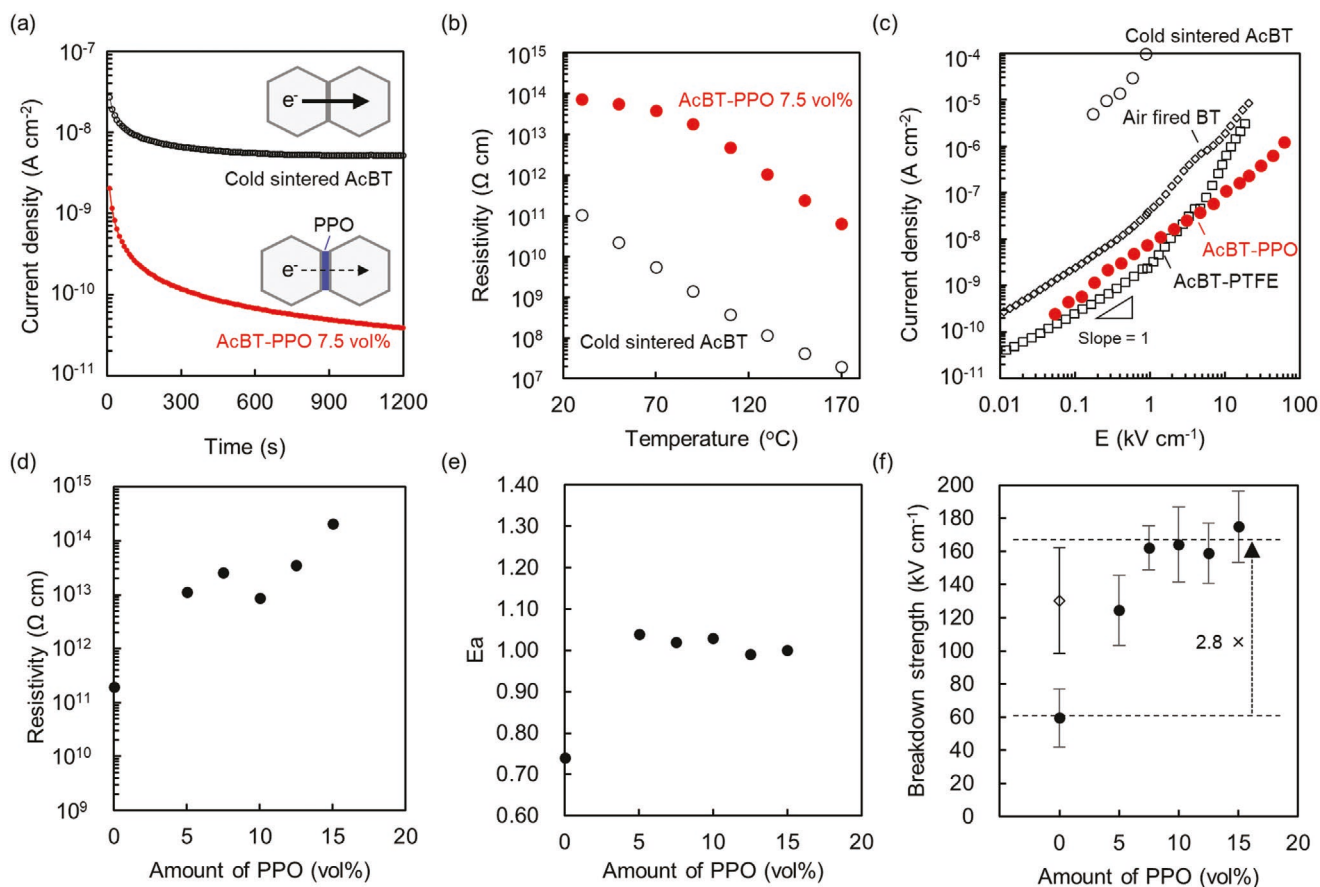


Figure 6. a) Changes in current density with time, b) temperature dependence of the resistivity, and c) Current density – Electric field (I - V) characteristics at 150 °C for the cold sintered AcBT (black open circles) and the composite with 7.5 vol% PPO (red solid circles). I - V characteristics for the composite with 5 vol% PTFE (open squares) and the conventionally air sintered BaTiO₃ ceramics (open diamonds) are also shown in (c). d) Resistivity, e) activation energy extracted in the natural logarithm Arrhenius plots using (b), and f) the electrical breakdown strength (BDS) for the composites as a function of volume fraction of PPO. BDS for the conventionally air sintered BT ceramics of similar density and thickness (open diamonds) are also shown in (f).

12.5, and 15 vol%. The intermediate relative permittivity for the PPO 7.5 vol% is almost linear and low loss dielectrics out to field amplitudes to 40 kV cm⁻¹ above the coercive field for typical ceramic BaTiO₃ dielectrics.

The electrical properties of the AcBT-PPO are also considered and compared to the BT-PTFE and a conventional air-fired BT dielectric. **Figure 6a** shows the development of the steady-state current on application of a voltage with time. The initial time is consistent with the change in current with time described by the Curie-Von Schweidler equation.^[60] This is regarded as a fundamental theory that describes the depolarization current in a dielectric material after a constant field, E , is either rapidly applied or removed. The general form of the variation of the current density, J , with time is given by $J(t) = kt^{-n}$ ($0 < n < 1$). A long decay is characteristic of highly insulating materials, and it is important to determine the resistivity when the depolarization discharge no longer impacts the steady state current, so we must wait for long times in these highly resistive dielectrics. The resistivity, ρ , in the AcBT-PPO for greater than 5 vol%, has resistivity $\approx 10^{13}$ to 10^{14} Ω cm at room temperature, as shown in **Figure 6d**. As a function of applied electric field at 150 °C, we see that at higher fields, both the conventional air-fired BT and the BT-PTFE composites have the onset of a non-

linear conduction mechanism as fields approach 5 kV cm⁻¹, as shown in **Figure 6c**. In the nanocomposite with 7.5 vol% PPO, these nonlinear conductive mechanisms are suppressed to far higher field, and there is Ohmic conduction ($J = \sigma E$, σ : electrical conductivity) up to an average field of 80 kV cm⁻¹ at 150 °C, therefore leading a much lower current density. The suppression of the non-linear conduction mechanisms is owing to the local field distribution being more directed to the highly insulative PPO grain boundaries. In principle, the same effects should be observed in the PTFE case, but the poorer distribution through the microstructure is associated with the lower performance of the PTFE relative to the AcBT-PPO nanocomposites. **Figure 6b** shows a comparison of the resistivities as a function of temperature plotted, and the activated resistivity is consistent with the Arrhenius dependence. We can observe the increase in the activation energy (E_a) from 0.74 eV for cold sintered AcBT to ≈ 1.0 eV for the AcBT-PPO composite (**Figure 6e**), and it is essentially invariant with the different volume fractions of PPO. **Figure 6f** show the breakdown strength (BDS) as a function of PPO amount. The Weibull plot is also shown in **Figure S7** in the Supporting Information. The BDS of the cold sintered AcBT is lower than that of conventional air-fired BT. However, with PPO greater than 7.5 vol%,

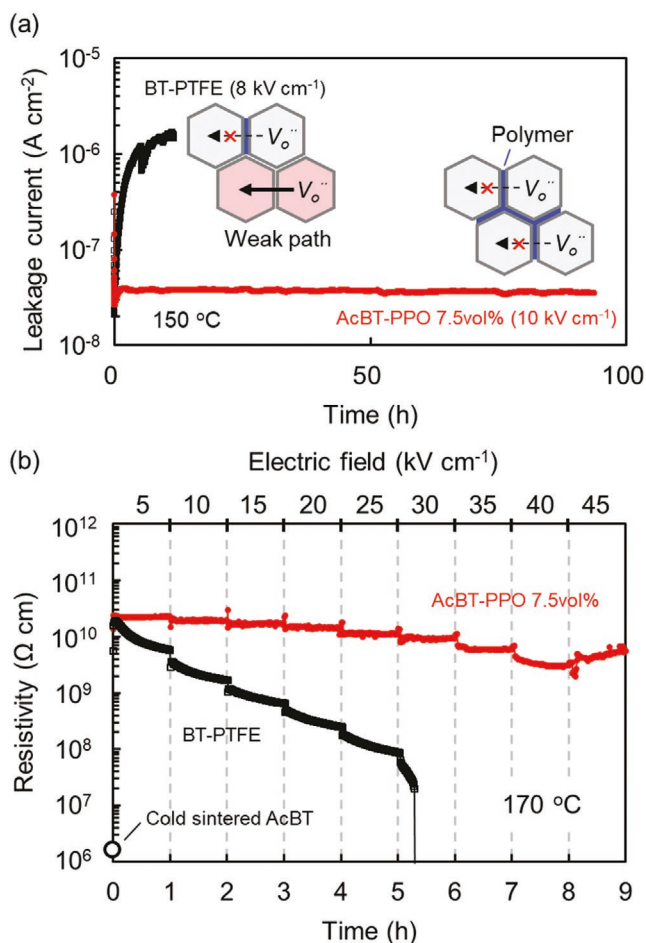


Figure 7. (single-column) Change in a) leakage current under a constant voltage at 150 °C and b) resistivities under voltage steps at 170 °C for the BT-PTFE (black) and AcBT-PPO composites (red). The applied fields in a) were 8 and 10 kV cm⁻¹ for the BT-PTFE and AcBT-PPO composites, respectively. The resistivity of cold sintered AcBT are also shown in (b).

the nanocomposites exhibit higher BDS than both of cold sintered and conventional air-fired BT.

The acid treated BaTiO₃ powders are used to improve the interaction between two phases, and polymer distribution. When we used BaTiO₃ powders without acid treatment, we found significant difference in the relative density, dielectric constant, and high temperature resistivity at high fields, as can be seen in Figure S8a–c in the Supporting Information. In addition to the discussion with BT-PTFE composites, these results also highlight the importance of improving the spatial distribution of polymer phase in the oxides.

As mentioned in the introduction, the time dependent degradation of a dielectric is a concern in the development of high field, high temperature dielectrics. The major mechanism is the electromigration of oxygen vacancies that migrate under the bias towards the cathode. In Figure 7a, it is shown that the change in current as a function of time under a high field and at a temperature of 150 °C, in comparison to the AcBT – PPO, and BT – PTFE composites. We see that with BT – PTFE, the degradation sets in after few hours; however, in the case of the AcBT-PPO, this is very much suppressed. In principle,

the PTFE in the grain boundary should be effective to the migration of oxygen vacancies, but the inhomogeneous spatial distribution of the PTFE across each grain boundary limits the degradation performance. Without polymers in grain boundaries, the local fields will not be confined to the grain boundary, and so the vacancies will migrate and transcend the grain boundaries, then percolation pathways around those regions without polymer will lead to the observed degradation. In contrast, the controlled PPO physical adsorption on the BaTiO₃ particles provides a uniform distribution of polymer in the final cold sintered AcBT-PPO nanocomposites, and thereby these weak-link regions of high field concentration in BaTiO₃ grains are vastly minimized. In addition to the accelerated lifetime test, we also consider the suppression of the vacancy migration with time with a systematic increase and hold of applied fields at a temperature of 170 °C. This type of degradation was earlier used by Yoon et al. on base metal dielectrics to access the resilience of a dielectric under high dielectric stresses.^[61] Figure 7b also shows the high performance with the AcBT-PPO dielectrics under these studies, with a field being applied as high as 45 kV cm⁻¹ @170 °C, increased at these higher fields sequentially every hour. We can see that on every increase in field at each hour, there is a depolarization relaxation, and at the longer times and higher fields, the data become noisier, but the stability is remarkable in comparison to the BT – PTFE composites. Compared with other conventional polymer-based composites (Table S1), our approach enables us to fabricate the dense ceramic-polymer nanocomposite without compromising high permittivity but also enhancing reliability.

2.4. Grain Boundary Design Strategy for High Permittivity Dielectrics

Ever since the introduction of cold sintering in 2016,^[18] we have looked to integrate novel materials into grain boundaries to obtain new advantages in material design. In this investigation, we have improved the dispersion of a polymer (PPO) and used a physical adsorption process to achieve the homogeneous distribution throughout the microstructure without hindering the densification. The superior distribution of the PPO is reflected in the variation of the permittivity with PPO volume fraction, along with the suppression of the non-linear dielectric behavior, suppression of non-linear conductivity, and improved resistance to degradation under accelerated lifetime testing conditions. In the supplemental data Table S1 shows a comparison of the dielectric permittivity properties for BaTiO₃ and polymer composites. It can be seen that relative to the prior literature, the relative permittivity for the composites is a major improvement over the earlier methods of developing polymer-BaTiO₃ composites, with various volume fractions, dispersion strategies, BaTiO₃ particle sizes, and polymer chemistries.

Although, the work here was only demonstrated on pellet samples (0.5 – 1 mm thickness), we can consider the possible advantages of taking this technology to a dielectric layer (less than 50 μm) in a multilayer capacitor device. We would expect that higher electric field can be applied, with higher breakdown strengths with thinner layers, recalling that breakdown strengths (E_b) are often controlled by extrinsic mechanisms

and show the empirical power law dependence upon dielectric thicknesses (d), given by $E_b = A \times d^{-n}$, where A is a constant and the exponent n varies depending on the materials and thickness range.^[62,63] This being the case, with the continued suppression of the high fields in the grains, we could also see major advantages, with the high permittivity, and suppressed voltage saturation effects towards high energy density capacitors. The electrostatic energy density, W_E are given by

$$W_E = \int_0^{E_{\max}} E dP = \int_0^{E_{\max}} \epsilon_0 \epsilon_r E dE \quad (2)$$

In the case of a linear dielectric, $W_E = 1/2 \epsilon_0 \epsilon_r E^2$, the linear dielectrics are often having low permittivity. There have been many efforts to overcome this by using relaxor polymer ferroelectrics, or suppressing voltage saturation in high permittivity dielectrics, or using phase change materials such as antiferroelectric materials, that increase permittivity. The new design obtained here would provide a new class of dielectric materials with both high performance and high reliability in the cutting edge electronic devices.

3. Conclusions

This study highlighted important steps to fabricate BaTiO₃-PPO nanocomposite with improved distribution of PPO in grain boundaries. The powder processing involves an acidic treatment of BaTiO₃ surface, followed by physisorption of PPO polymers by simple mixing. These powders were cold sintered at 225 °C and 350 MPa to obtain high-density dielectrics nanocomposites. The dielectric properties of cold sintered nanocomposites are controlled with a redistribution of local electric fields that suppress many of the deleterious mechanisms that limit high permittivity dielectrics. Key additional properties that have been highlighted include: (i) Composites with high relative permittivity ≈ 1000 – 2000 , and a dielectric loss tangent ≈ 0.05 ; (ii) Reduced temperature dependence of the permittivity with diffuse phase transitions, over a broad temperature window; (iii) High resistivities, ρ , $\approx 10^{13}$ – 10^{14} Ω cm at room temperature; (iv) Suppressed non-linear voltage saturation effects under high applied fields, $\epsilon_r(E) \approx$ constant; (v) Suppressed non-linear conductivity to high fields (≈ 80 kV cm⁻¹) and high temperatures ≈ 150 °C, $J \approx \sigma E$; and (vi) Suppressed degradation rates with the polymer barriers at the grain boundary. These extremely interesting properties can offer many new dielectrics design opportunities, along with many scientific investigations on the natures of the ferroelectric behavior, and conduction behavior under highly localized electric field distribution.

4. Experimental Section

Materials: The basic BaTiO₃ powders synthesized with the typical oxalate method were supplied by Kyocera (Kagoshima, Japan). The cold sintering transient phase was selected to be barium hydroxide octahydrate (> 98%), and this was purchased from Alfa Aesar and used as received. Micro-fine polytetrafluoroethylene (PTFE) was obtained from Howard P. Industries. Poly(2,6-dimethyl-1,4-phenylene oxide) (PPO) was purchased from Sigma Aldrich.

Powder Preparation: The as-received BaTiO₃ powder was first calcined at 700 °C for 1 h to completely remove organic residues, including oxycarbonates. The calcined BaTiO₃ powder (4.0 g) was mixed with a 1 M acetic acid aqueous solution (20 mL) at 80 °C for 1 h for further BaTiO₃ surface preparation. This drives an incongruent dissolution, depleting the surfaces of Ba-ions and leaving an amorphous Ti-oxide passivated layer. After the treatment, the powder was collected by filtration (EZFlow PES membrane, 0.22 μ m), washed with deionized water, and dried at 80 °C in vacuum for 24 h.

PPO Solution: 0.15 g of PPO was added in 10 mL of toluene and stirred at 80 °C until the PPO was completely dissolved. The PPO solution was stored in a vial with parafilm sealing film.

CSP of BaTiO₃ – PPO Composite: PPO solution with a given volume was added to 0.75 g of acid-treated BaTiO₃ using micropipette and homogeneously mixed using a pestle and mortar until toluene was evaporated. The volume fraction of PPO was 5, 7.5, 10, 12.5 and 15 vol%. After drying completely, 0.11 g of Ba(OH)₂·8H₂O was added to the mixture and homogeneously ground and mixed using a pestle and mortar prior to sintering. The mixture was loaded into a 12.7 mm diameter die and uniaxially pressed under 350 MPa. Since the melting point of Ba(OH)₂·8H₂O is 78 °C, a pre-heating step was conducted at 80 °C for 0.5 h to allow its homogeneous distribution in the BaTiO₃ powder. Then, the set temperature was increased to 225 °C, using both a heater jacket and a press equipped with hot plates and held for 1.5 h under 350 MPa. The pressure was applied before ramping up and released immediately after the dwell time. The as-prepared samples after cold sintering were dried under N₂ flow at 200 °C for 12 h and stored in an oven at 120 °C to prevent the water absorption. As a reference sample, BaTiO₃ ceramics were also prepared by the conventional solid-state high-temperature sintering. The initial BaTiO₃ ceramic powder was mixed with the binder solution (5 wt% of Acryloid B72 and 95 wt% of acetone). The ratio of the binder to BaTiO₃ was adjusted to 2 wt%. The slurry was then dried at 50 °C with stirring by magnetic stirrer. The dried powder was sieved and pressed into pellets. The green pellets were heated to 600 °C for 2 h to remove the organic binder, then heated to 1260 °C for 2 h with the heating rate of 5 °C min⁻¹.

Materials Characterization: To investigate the interaction between PPO and BaTiO₃ (BT), Fourier Transformed Infrared Spectroscopy (FTIR) experiments were conducted using a Bruker Vertex 70 FTIR spectrometer (Billerica) with an Attenuated Total Reflection (ATR) accessory, equipped with a liquid nitrogen-cooled MCT detector. Spectra were collected at room temperature and were obtained from an average of 200 scans in the wavelength range of 500–4000 cm⁻¹. Additional analysis of PPO adsorption was performed with a spectroscopic UV–vis method and using the KM function (Lambda 950 UV–vis Spectrophotometer, Perkin-Elmer).

Bulk densities (ρ_b) were obtained by Archimedes method, performed using ethanol. Theoretical densities were calculated using a volumetric mixing law from contributing compounds BaTiO₃ (6.03 g cm⁻³) and PPO (1.06 g cm⁻³). The relative density was then calculated from the ρ_b/ρ_{th} ratio. X-ray diffraction (XRD) was measured at 45 kV and 40 mA with Cu-K α radiation (Empyrean, Malvern Panalytical). Diffraction patterns were collected at 2θ angles between 10° and 70° with a step size of 0.026° and a scan rate of 0.067° s⁻¹, using bulk samples carefully polished with different grit papers (sizes #320, 600, 800, and 1200). Scanning electron microscopy (SEM) images of microstructure with sputtered iridium were observed using fracture surface of the samples at an accelerating voltage of 5 kV (Apreo SEM, Thermo Scientific). For the electrical property measurements, 80 nm-thick Pt electrodes were deposited by sputtering (Q150R Plus, Quorum Technologies) on polished surfaces. Dielectric properties were measured at 1 kHz in the temperature range between –20 and 170 °C using LCR meter (E4980A, Agilent Technologies). To investigate the stability of the dielectric properties, the samples were placed under ambient laboratory conditions for 48 h. The measurement for 0 h was conducted immediately after drying at 120 °C in an oven. The temperature dependence of the resistivity was measured by applying a fixed dc electric field of 1 kV cm⁻¹ for 3 min at each step of the temperature using HP 4140B pA meter. The

current-voltage (*I-V*) characteristics of BaTiO₃-PPO composites were measured by the two-probe method, using HP 4140B pA meter with Trek Model 610D high voltage amplifier system. To investigate the degradation, the leakage currents were measured at 150 °C with a fixed DC electric field of 10 kV cm⁻¹ for BaTiO₃-PPO composite and 0.8 kV cm⁻¹ for BaTiO₃-PTFE composite and conventional air-fired BaTiO₃ using a power supply/amplifier (Model BOP 1000, KEPC) and a multimeter/data acquisition system (2700, Keithley Instruments). DC breakdown test were performed with 500 V s⁻¹ ramp on 0.5 mm thick samples using a high voltage power source (Model 30/20, TRek) at room temperature.

Transmission electron microscopy (TEM) for high-resolution microstructure analysis was measured at 200 kV (TALOS F200X, FEI, USA), on powders dispersed on a holey carbon grid, with observations made with particles overlapping the holes. Scanning transmission electron microscopy – energy dispersive spectroscopy (STEM-EDS) was performed using a SuperX EDS system to collect elemental information in the ACBT powders with PPO coating.

Supporting Information

Supporting Information is available from the Wiley Online Library or from the author.

Acknowledgements

T.S. would like to thank Kyocera Corporation for a Visiting Scientist Research Fellowship to Penn State and the Center for Dielectrics and Piezoelectrics. A.N., Z.F., and C.R. thanks the AFOSR grant (no. FA9550-19-1-0372) and the support and suggestions of the Program Manager. The authors also wish to thank the staffs of the MCL for aid in sample preparation and in maintaining electrical measurement facilities. They also thank Joanne Aller for helping in proof reading and formatting this publication.

Conflict of Interest

The authors declare no conflict of interest.

Data Availability Statement

The data that supports the findings of this study are available in the supplementary material of this article.

Keywords

capacitors, ceramic-polymer composites, cold sintering, dielectrics, ferroelectrics

Received: June 9, 2021

Revised: July 15, 2021

Published online: August 31, 2021

- [1] K. Hong, T. H. Lee, J. M. Suh, S.-H. Yoon, H. W. Jang, *J. Mater. Chem. C* **2019**, *7*, 9782.
 [2] J. Bultitude, J. McConnell, C. Shearer, *J. Mater. Sci. Mater. Electron.* **2015**, *26*, 9236.
 [3] J. Watson, G. Castro, *J. Mater. Sci. Mater. Electron.* **2015**, *26*, 9226.

- [4] Z. Yao, Z. Song, H. Hao, Z. Yu, M. Cao, S. Zhang, M. T. Lanagan, H. Liu, *Adv. Mater.* **2017**, *29*, 1601727.
 [5] Prateek, R. Bhunia, A. Garg, R. K. Gupta, *J. Phys. Chem. C* **2020**, *124*, 22914.
 [6] Prateek, R. Bhunia, S. Siddiqui, A. Garg, R. K. Gupta, *ACS Appl. Mater. Interfaces* **2019**, *11*, 14329.
 [7] R. Waser, T. Baiatu, K.-H. Härdtl, *J. Am. Ceram. Soc.* **1990**, *73*, 1645.
 [8] R. Waser, T. Baiatu, K.-H. Härdtl, *J. Am. Ceram. Soc.* **1990**, *73*, 1654.
 [9] T. Baiatu, R. Waser, K.-H. Härdtl, *J. Am. Ceram. Soc.* **1990**, *73*, 1663.
 [10] M. Randall, D. Skamser, T. Kinard, J. Qazi, A. Tajuddin, S. Trolier-McKinstry, C. Randall, S. W. Ko, T. Dechakupt, in *CARTS 2007 Symp. Proc.*, Albuquerque, NM, **2007**, pp. 1–12.
 [11] H. Kishi, Y. Mizuno, H. Chazono, *Jpn. J. Appl. Phys.* **2003**, *42*, 1.
 [12] B. Jiang, J. Iocozzia, L. Zhao, H. Zhang, Y.-W. Harn, Y. Chen, Z. Lin, *Chem. Soc. Rev.* **2019**, *48*, 1194.
 [13] D.-H. Yoon, B. I. Lee, *J. Eur. Ceram. Soc.* **2004**, *24*, 753.
 [14] M. M. Samantaray, K. Kaneda, W. Qu, E. C. Dickey, C. A. Randall, *J. Am. Ceram. Soc.* **2012**, *95*, 992.
 [15] M. Pan, C. A. Randall, *IEEE Electr. Insul. Mag.* **2010**, *26*, 44.
 [16] M. H. Lee, D. J. Kim, J. S. Park, S. W. Kim, T. K. Song, M.-H. Kim, W.-J. Kim, D. Do, I.-K. Jeong, *Adv. Mater.* **2015**, *27*, 6976.
 [17] Y. Wang, W. Jie, C. Yang, X. Wei, J. Hao, *Adv. Funct. Mater.* **2019**, *29*, 1808118.
 [18] J. Guo, H. Guo, A. L. Baker, M. T. Lanagan, E. R. Kupp, G. L. Messing, C. A. Randall, *Angew. Chem., Int. Ed.* **2016**, *55*, 11457.
 [19] S. Dursun, K. Tsuji, S. H. Bang, A. Ndayishimiye, C. A. Randall, *ACS Appl. Electron. Mater.* **2020**, *2*, 1917.
 [20] J. A., D. B., I. M. Reaney, *Johnson Matthey Technol. Rev.* **2020**, *64*, 219.
 [21] D. Zou, Y. Fan, *Ceram. Int.* **2021**.
 [22] T. Ibn-Mohammed, C. A. Randall, K. B. Mustapha, J. Guo, J. Walker, S. Berbano, S. C. L. Koh, D. Wang, D. C. Sinclair, I. M. Reaney, *J. Eur. Ceram. Soc.* **2019**, *39*, 5213.
 [23] J. Guo, X. Zhao, T. Herisson De Beauvoir, J.-H. Seo, S. S. Berbano, A. L. Baker, C. Azina, C. A. Randall, *Adv. Funct. Mater.* **2018**, *28*, 1801724.
 [24] J. Guo, B. Legum, B. Anasori, K. Wang, P. Lelyukh, Y. Gogotsi, C. A. Randall, *Adv. Mater.* **2018**, *30*, 1801846.
 [25] T. Sada, K. Tsuji, A. Ndayishimiye, Z. Fan, Y. Fujioka, C. A. Randall, *J. Eur. Ceram. Soc.* **2021**, *41*, 409.
 [26] T. Sada, K. Tsuji, A. Ndayishimiye, Z. Fan, Y. Fujioka, C. A. Randall, *J. Appl. Phys.* **2020**, *128*, 084103.
 [27] Z.-M. Dang, Y.-Q. Lin, H.-P. Xu, C.-Y. Shi, S.-T. Li, J. Bai, *Adv. Funct. Mater.* **2008**, *18*, 1509.
 [28] R. K. Goyal, V. V. Madav, P. R. Pakankar, S. P. Butee, *J. Electron. Mater.* **2011**, *40*, 2240.
 [29] D.-H. Kuo, C.-C. Chang, T.-Y. Su, W.-K. Wang, B.-Y. Lin, *Mater. Chem. Phys.* **2004**, *85*, 201.
 [30] R. Guo, J. I. Roscow, C. R. Bowen, H. Luo, Y. Huang, Y. Ma, K. Zhou, D. Zhang, *J. Mater. Chem. A* **2020**, *8*, 3135.
 [31] T. Sada, N. Fujikawa, *Jpn. J. Appl. Phys.* **2017**, *56*, 10PB04.
 [32] K. Izawa, T. Sada, M. Utsunomiya, S. Inayama, N. Fujikawa, K. Matsubara, K. Yasukawa, *Appl. Phys. Lett.* **2020**, *116*, 192903.
 [33] F. E. Bouharras, M. Raihane, B. Ameduri, *Prog. Mater. Sci.* **2020**, *113*, 100670.
 [34] Y. Chen, M. Xu, X. Li, J. Liu, N. Zhu, M. Zhang, W. Ma, Z. Shi, J. Zhang, X. Lu, X. Zhang, *ACS Appl. Energy Mater.* **2021**, *4*, 470.
 [35] M. Zhu, X. Huang, K. Yang, X. Zhai, J. Zhang, J. He, P. Jiang, *ACS Appl. Mater. Interfaces* **2014**, *6*, 19644.
 [36] P. Kim, S. C. Jones, P. J. Hotchkiss, J. N. Haddock, B. Kippelen, S. R. Marder, J. W. Perry, *Adv. Mater.* **2007**, *19*, 1001.
 [37] P. Kim, N. M. Doss, J. P. Tillotson, P. J. Hotchkiss, M.-J. Pan, S. R. Marder, J. Li, J. P. Calame, J. W. Perry, *ACS Nano* **2009**, *3*, 2581.
 [38] Y. Niu, Y. Bai, K. Yu, Y. Wang, F. Xiang, H. Wang, *ACS Appl. Mater. Interfaces* **2015**, *7*, 24168.

- [39] Y. Niu, F. Xiang, Y. Wang, J. Chen, H. Wang, *Phys. Chem. Chem. Phys.* **2018**, *20*, 6598.
- [40] B. Luo, X. Wang, Y. Wang, L. Li, *J. Mater. Chem. A* **2014**, *2*, 510.
- [41] M.-F. Lin, V. K. Thakur, E. J. Tan, P. S. Lee, *RSC Adv.* **2011**, *1*, 576.
- [42] T. Sada, A. Ndayishimiye, Z. Fan, Y. Fujioka, C. A. Randall, *J. Appl. Phys.* **2021**, *129*, 184102.
- [43] T. Zhou, J.-W. Zha, R.-Y. Cui, B.-H. Fan, J.-K. Yuan, Z.-M. Dang, *ACS Appl. Mater. Interfaces* **2011**, *3*, 2184.
- [44] M. N. Almadhoun, U. S. Bhansali, H. N. Alshareef, *J. Mater. Chem.* **2012**, *22*, 11196.
- [45] L. Shaohui, Z. Jiwei, W. Jinwen, X. Shuangxi, Z. Wenqin, *ACS Appl. Mater. Interfaces* **2014**, *6*, 1533.
- [46] G. Merle, M. Wessling, K. Nijmeijer, *J. Membr. Sci.* **2011**, *377*, 1.
- [47] Adsorption of Polymers at Solid Surfaces, **2014**, pp. 211–229.
- [48] T. Sada, Z. Fan, A. Ndayishimiye, K. Tsuji, S. H. Bang, Y. Fujioka, C. A. Randall, *J. Am. Ceram. Soc.* **2021**, *104*, 96.
- [49] D. Völtzke, H.-P. Abicht, J. Woltersdorf, E. Pippel, *Mater. Chem. Phys.* **2002**, *73*, 274.
- [50] C.-C. Li, S.-J. Chang, J.-T. Lee, W.-S. Liao, *Colloids Surf A: Physicochem. Eng. Asp.* **2010**, *361*, 143.
- [51] S.-J. Chang, W.-S. Liao, C.-J. Ciou, J.-T. Lee, C.-C. Li, *J. Colloid Interface Sci.* **2009**, *329*, 300.
- [52] R. E. Riman, W. L. Suchanek, M. M. Lencka, *Ann. Chim. Sci. des Matériaux* **2002**, *27*, 15.
- [53] T. Xu, Z. Liu, Y. Li, W. Yang, *J. Membr. Sci.* **2008**, *320*, 232.
- [54] C. Gong, R. Guan, Y.-C. Shu, F.-S. Chuang, W.-C. Tsen, *Polym. Adv. Technol.* **2007**, *18*, 44.
- [55] S. Mathur, B. M. Moudgil, *J. Colloid Interface Sci.* **1997**, *196*, 92.
- [56] Y. Wu, C. Wu, T. Xu, X. Lin, Y. Fu, *J. Membr. Sci.* **2009**, *338*, 51.
- [57] T. Hérisson de Beauvoir, K. Tsuji, X. Zhao, J. Guo, C. Randall, *Acta Mater.* **2020**, *186*, 511.
- [58] A. Ndayishimiye, K. Tsuji, K. Wang, S. H. Bang, C. A. Randall, *J. Eur. Ceram. Soc.* **2019**, *39*, 4743.
- [59] A. D. Mohanty, S. E. Tignor, J. A. Krause, Y.-K. Choe, C. Bae, *Macromolecules* **2016**, *49*, 3361.
- [60] T. C. Guo, W. W. Guo, *J. Phys. C Solid State Phys.* **1983**, *16*, 1955.
- [61] S.-H. Yoon, C. A. Randall, K.-H. Hur, *J. Appl. Phys.* **2010**, *108*, 064101.
- [62] H. Y. Lee, K. H. Cho, H.-D. Nam, *Ferroelectrics* **2006**, *334*, 165.
- [63] A. D. Milliken, A. J. Bell, J. F. Scott, *Appl. Phys. Lett.* **2007**, *90*, 112910.